

## Combining deep learning and coherent anti-Stokes Raman scattering imaging for automated differential diagnosis of lung cancer

Sheng Weng  
Xiaoyun Xu  
Jiasong Li  
Stephen T. C. Wong

# Combining deep learning and coherent anti-Stokes Raman scattering imaging for automated differential diagnosis of lung cancer

Sheng Weng,<sup>a,b</sup> Xiaoyun Xu,<sup>a</sup> Jiasong Li,<sup>a</sup> and Stephen T. C. Wong<sup>a,b,\*</sup>

<sup>a</sup>Translational Biophotonics Laboratory, Department of Systems Medicine and Bioengineering, Houston Methodist Research Institute, Weill Cornell Medicine, Houston, Texas, United States

<sup>b</sup>Rice University, Department of Electrical and Computer Engineering, Houston, Texas, United States

**Abstract.** Lung cancer is the most prevalent type of cancer and the leading cause of cancer-related deaths worldwide. Coherent anti-Stokes Raman scattering (CARS) is capable of providing cellular-level images and resolving pathologically related features on human lung tissues. However, conventional means of analyzing CARS images requires extensive image processing, feature engineering, and human intervention. This study demonstrates the feasibility of applying a deep learning algorithm to automatically differentiate normal and cancerous lung tissue images acquired by CARS. We leverage the features learned by pretrained deep neural networks and retrain the model using CARS images as the input. We achieve 89.2% accuracy in classifying normal, small-cell carcinoma, adenocarcinoma, and squamous cell carcinoma lung images. This computational method is a step toward on-the-spot diagnosis of lung cancer and can be further strengthened by the efforts aimed at miniaturizing the CARS technique for fiber-based microendoscopic imaging. © The Authors. Published by SPIE under a Creative Commons Attribution 3.0 Unported License. Distribution or reproduction of this work in whole or in part requires full attribution of the original publication, including its DOI. [DOI: [10.1117/1.JBO.22.10.106017](https://doi.org/10.1117/1.JBO.22.10.106017)]

Keywords: nonlinear microscopy; medical imaging; lung cancer; classification; artificial intelligence; deep learning.

Paper 170444RR received Jul. 7, 2017; accepted for publication Oct. 4, 2017; published online Oct. 30, 2017.

## 1 Introduction

Lung cancer is responsible for the most cancer-related deaths in the world. In 2017, it is estimated that there will be 222,500 cases of lung cancer and 155,870 deaths from lung cancer in the United States.<sup>1</sup> Despite the steady increase in survival for most cancers in recent years, advance has been slow for lung cancer, resulting in only 18% 5-year survival rate.<sup>1,2</sup> This low rate is partly due to the asymptomatic nature of lung lesions,<sup>3</sup> which prevents lung cancer from being diagnosed at an earlier stage.<sup>4</sup> There are two main types of lung cancer: about 80% to 85% of lung cancer is nonsmall cell lung cancer (NSCLC), the remaining forms are small-cell lung cancer. Adenocarcinoma and squamous cell carcinoma are the two major subtypes of NSCLC. Adenocarcinoma is the most common form of lung cancer that accounts for about 40% of total lung cancer incidences. Squamous cell carcinoma accounts for about 30% of total lung cancer incidences, and they are often linked to a history of smoking. Currently, a computed tomography (CT)-guided fine needle biopsy is the standard routine for pathological analysis and definitive diagnosis of lung cancer.<sup>5,6</sup> Although CT-guided fine needle aspiration can reduce the amount of tissue taken and complications, because of the limited resolution of CT scans and the respiratory motion of patients, it is sometimes difficult to obtain samples precisely at the site of neoplastic lesions and thus the correct diagnosis.<sup>7</sup> Some patients will have to undergo rebiopsy, resulting in increased costs and delay in diagnosis and definitive treatment. Therefore, it would be beneficial to develop

techniques that allow medical practitioners to detect and diagnose lung cancer with high speed and accuracy.

In recent years, although needle biopsy and pathology analysis still remain the gold standard for definitive lung cancer diagnosis, rapid development in nonlinear optical imaging technologies has contributed to advancing diagnostic strategies in cancer, including autofluorescence bronchoscopy,<sup>8–10</sup> two-photon-excited fluorescence microscopy,<sup>11,12</sup> and optical coherence tomography.<sup>13–15</sup> Our group has previously demonstrated the use of coherent anti-Stokes Raman scattering (CARS) imaging as a fast and accurate differential diagnostic tool for the detection of lung cancer.<sup>16–18</sup> CARS is an emerging label-free imaging technique that captures intrinsic molecular vibrations and offers real-time submicron spatial resolution along with information of the biological and chemical properties of samples, without applying any exogenous contrast agents that may be harmful to humans.<sup>19</sup> In CARS, two laser beams are temporally and spatially overlapped at the sample to probe designated molecular vibrations and produce signals through a four-wave mixing process<sup>19</sup> in a direction determined by the phase-matching conditions.<sup>20</sup> When the frequency difference between the pump field and the Stokes field matches the vibrational frequency of Raman active molecules in the sample, the resonant molecules are coherently driven to an excited state and then generate CARS signals that are typically several orders of magnitude stronger than conventional spontaneous Raman scattering.<sup>21</sup> We have shown that CARS can offer cellular resolution images of both normal and cancerous lung tissue where pathologically related features can be clearly revealed.<sup>16</sup> Based on the extracted quantitative features describing fibrils and cell morphology, we have developed a knowledge-based classification platform to differentiate cancerous from

\*Address all correspondence to: Stephen T. C. Wong, E-mail: [STWong@houstonmethodist.org](mailto:STWong@houstonmethodist.org)

normal lung tissues with 91% sensitivity and 92% specificity. Small-cell carcinoma was distinguished from NSCLC with 100% sensitivity and specificity.<sup>18</sup> Since CARS has the capability to provide three-dimensional (3-D) images, we have also designed a superpixel-based 3-D nuclear segmentation and clustering algorithm<sup>22–24</sup> to characterize NSCLC subtypes. The result showed greater than 97% accuracy in separating adenocarcinoma and squamous cell carcinoma.<sup>17</sup>

The above-mentioned classification algorithms, however, require extensive image preprocessing, nuclei segmentation, and feature extraction based on the cellular and fibril structural information inherent in CARS images. A total of 145 features was directly calculated from the CARS images to separate fibril-dominant normal from cell-dominant cancerous lung lesions.<sup>18</sup> A semiautomatic nuclei segmentation algorithm was implemented to facilitate the measurement of morphological features that describe both the attributes of individual cells and their relative spatial distribution, such as cell volume, nuclear size, and distance between cells.<sup>25</sup> Thirty-five features were extracted based on the segmentation result to distinguish cancerous lung lesions. Partial least squares regression<sup>26</sup> and a support vector machine<sup>27</sup> were employed as the classification algorithms. Aiming at improving the classification accuracy of the two subtypes of NSCLC, we extended the two-dimensional (2-D) analytical framework to a 3-D nuclear segmentation, feature extraction, and classification system. This diagnostic imaging system involved partitioning the image volume into supervoxels and manually selecting the cell nuclei.<sup>28</sup> Another thirty-two features were computed to build a classifier capable of differentiating adenocarcinoma and squamous cell carcinoma lung cancer subtypes.<sup>17</sup>

To circumvent the complex image processing and feature engineering procedure and avert any possible human interventions, in this paper, we demonstrate the classification of CARS images on lung tissues using a deep convolutional neural network (CNN) that needs no hand-crafted features.<sup>29–34</sup> Deep learning algorithms, powered by advances in computation and very large datasets, have recently been shown to be successful in various tasks.<sup>35–39</sup> CNN is effective for image classification problems because the nature of weight sharing produces information on spatially correlated features of the image. Since training a deep CNN from scratch is computationally expensive and time-consuming, we apply a transfer learning approach that takes advantage of the weights of a pretrained model named GoogleNet Inception v3, which was pretrained on ~1.28 million images (1000 object categories) from the 2014 ImageNet large-scale visual recognition challenge and achieved 5.64% top-5 error.<sup>40–45</sup> To the best of our knowledge, the characterization of CARS or other label-free microscopic images using deep CNN has not been attempted. Combining the label-free high-resolution imaging modality and deep learning image classification algorithm will lead to a strategy of automated differential diagnosis of lung cancer.

## 2 Materials and Methods

### 2.1 Tissue Sample Preparation

Fresh human lung tissues were obtained from patients undergoing lung surgery at Houston Methodist Hospital, Houston, Texas, approved by the Institutional Review Board. The excised tissues were immediately snap-frozen in liquid nitrogen for storage. Frozen tissue samples were passively thawed for 30 min at room temperature, placed on a 170- $\mu$ m cover slide (VWR,

Radnor, Pennsylvania), and then reversely placed on an imaging chamber to keep the samples from being pressed. CARS images were acquired *ex vivo* using a modified confocal microscope. Each lung tissue was imaged at several different locations, and at each location a series of images was acquired at different image depths, called a *z*-stack.<sup>46</sup> Each *z*-stack was considered as an independent sample. A total of 388 *z*-stacks (7926 images) was collected, including 83 (1920 images) normal cases, 156 (2618 images) adenocarcinoma cases, 111 (2535 images) squamous cell carcinoma cases, and 38 (853 images) small-cell carcinoma cases. Small-cell carcinoma cases are seldom resected clinically, resulting in a lower number. After experiments, all samples were marked to indicate the imaged locations, fixed with 4% neutral-buffered formaldehyde, embedded in paraffin, sectioned through imaged locations, and stained with hematoxylin and eosin (H&E). Bright-field images of the H&E slides were examined by pathologists with an Olympus BX51 microscope. Pathologists labeled the tissue based on the H&E-sectioning results, which was then used as the ground truth for the CARS images. Each tissue has only one specific label, i.e., we did not use tissues that might have both normal and tumor cells.

### 2.2 Coherent Anti-Stokes Raman Scattering Imaging System

The schematic of the CARS imaging system was previously described.<sup>16</sup> The light sources include a mode-locked Nd:YVO<sub>4</sub> laser (High-Q Laser, Hohenems, Austria) that delivers a 7-ps, 76-MHz pulse train at 1064 nm used as the Stokes beam, and a frequency-doubled pulse train at 532 nm, which is used to pump a tunable optical parametric oscillator (OPO, Levante, APE, Berlin, Germany) to generate the 5-ps pump beam at 817 nm. The resulting CARS signal is at 663 nm, corresponding to the CH<sub>2</sub> stretch vibration mode (2845 cm<sup>-1</sup>). The Stokes and pump laser beams are spatially overlapped using a long-pass dichroic mirror (q10201pxr, Chroma, Vermont) and temporally overlapped using an adjustable time-delay line. They are tightly focused by a 1.2-NA water immersion objective lens (60 $\times$ , IR UPlanApo, Olympus, Melville, New Jersey), yielding CARS signals with a lateral resolution of 0.4  $\mu$ m and an axial resolution of 0.9  $\mu$ m. A bandpass filter (hq660/40m-2p, Chroma Inc.) is placed before the photomultiplier tube (PMT, R3896, Hamamatsu, Japan) detector to block unwanted background signals. The PMT is designed to be most sensitive in the visible wavelength region. The upright microscope is modified from an FV300 confocal laser scanning microscope (Olympus, Japan) adopting a 2-D galvanometer. A dichroic mirror is used in the microscope to separate the CARS signals from excitation laser beams. The acquisition time is about 3.9 s per imaging frame of 512  $\times$  512 pixels. Image is displayed with the Olympus FluoView v5.0 software. The field of view (FOV) that we can normally achieve is 236  $\times$  236  $\mu$ m<sup>2</sup>. The average laser power is 75 mW for pump beam and 35 mW for Stokes beam, both within the safety range. In the human body, the tolerance to laser power is much higher than that in thawed tissues, therefore less photodamage is expected and the current laser power is expected to be suitable for clinical applications.<sup>47</sup>

### 2.3 Data Preparation

While CARS images corresponding to the same tissue but from different viewpoints look very different, a *z*-stack is likely to

contain similar images at different imaging depths, as the smallest  $z$ -step is only  $1\ \mu\text{m}$ . Therefore, extensive care was taken to ensure that images from the same  $z$ -stack were not split between the training and testing sets. We randomly picked eight normal lung  $z$ -stacks (160 images), 16 adenocarcinoma  $z$ -stacks (257 images), 12 squamous cell carcinoma  $z$ -stacks (239 images), and four small-cell carcinoma  $z$ -stacks (102 images) as our holdout test set. The rest of the dataset (7168 images) was used for training and validation. We converted our grayscale CARS images into RGB and resized each image to  $299 \times 299$  pixels as required by the pretrained model.

To facilitate the training of deep neural networks, a large amount of labeled data is normally needed. Unlike image databases, such as the ImageNet<sup>43</sup> and MS-COCO,<sup>48</sup> that are publicly available for the computer vision community, we have only a limited number of CARS images on human lung tissues, thus data augmentation was applied to prevent overfitting.<sup>49</sup> Overfitting occurs when a model is excessively complex as compared to the number of training data, so the model is not able to learn patterns that can generalize to new observations. Since tissues do not possess a particular orientation, performing augmentation with rotation and mirroring transformation should not alter the pathological information contained on the CARS images. Each image in the cross-validation set was augmented by a factor of 120 by randomly rotating the image 60 times and then flipping the rotated image horizontally. The cross-validation set contains 860,160 images after image augmentation. We did not use other augmentation methods that might involve artificial distortions on pixel values. The largest inscribed rectangle was then cropped from each image, resulting in an image with  $362 \times 362$  pixels.

## 2.4 Transfer Learning

Transfer learning refers to the process of using the knowledge learned on a specific task and adapting this knowledge to a different domain, based on the hypothesis that the features learned by the pretrained model are highly transferable.<sup>42,50</sup> Transfer learning reduces the time and computational resources needed to train deep neural networks from scratch on a large amount of data because it does not need to take time optimizing millions of parameters. Despite the disparity between natural images and

biological images, deep CNN architectures comprehensively trained on the large-scale well-annotated ImageNet can still be transferred to biological and medical domains and have demonstrated their successes in various image classification tasks, such as skin cancer,<sup>37</sup> colon polyps,<sup>51</sup> thyroid nodules,<sup>52</sup> thoraco-abdominal lymph nodes, and interstitial lung disease.<sup>53</sup> The GoogleNet Inception v3 model consists of 22 layers stacked on top of each other (see Fig. 1).<sup>40</sup> We replaced the final classification layer with four classes instead of the original 1000 ImageNet classes, the previous layers remained unchanged because the existing weights are already valuable at finding and summarizing features that are useful for image classification problems. Generally speaking, earlier layers in the model contain more general features, such as edge detectors or shape detectors, which should be ubiquitous for many image classification tasks, whereas later layers contain higher level features. We retrained the Inception v3 model using only pixels and labels of CARS images as inputs, and fine-tuned the final classification layer using a global learning rate of 0.05.

We randomly divided the training and validation set into nine partitions so that we could use ninefold cross validation to validate the performance of the algorithm. We then calculated and cached the bottleneck values for each image to accelerate the following training process. The bottleneck values are the information stored in the penultimate layer, which will be used multiple times during training.<sup>36</sup> In each step of training, the model selected a small batch of images at random, found their bottlenecks from the cache, and fed them into the final classification layer to perform prediction. Those predictions were then compared against the ground-truth labels to iteratively update the final layer's weights through backpropagation.<sup>55</sup> We used cross entropy as the cost function to measure the performance of our model. Smaller cross-entropy value means smaller mismatch between the predicted labels and the ground-truth labels. After 40,000 steps, the retrained model was evaluated on the holdout test set that was separated from the training and validation sets. All methods were implemented using Google's TensorFlow (version r1.1) deep learning framework<sup>56</sup> on Amazon Web Services (AWS) EC2 p2.xlarge instance, which contains 4 vCPU with 61 GiB memory and 1 GPU with 12 GiB memory. It took about 3 days to calculate and cache all the bottleneck

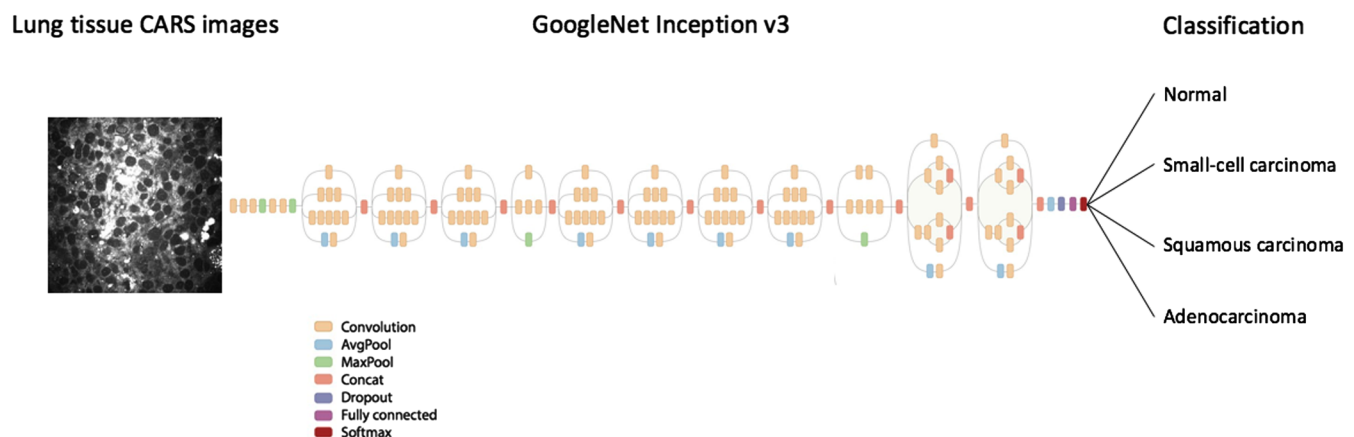


**Fig. 1** Transfer learning layout. Data flow is from left to right: a CARS image of human lung tissue is fed into GoogleNet Inception v3 CNN pretrained on the ImageNet data and fine-tuned on our own CARS images comprising four classes: normal, small-cell carcinoma, squamous carcinoma, and adenocarcinoma. The model outputs the probability distribution over the four classes and we label the CARS image with the largest probability class. GoogleNet Inception v3 CNN architecture reprinted from Ref. 54.



values for each image in the cross-validation set. After that, each cross-validation round took about half an hour, whereas the prediction on the holdout test set needed only 6 min.

### 3 Results

#### 3.1 Coherent Anti-Stokes Raman Scattering Imaging of Human Lung Tissues

Figure 2 represents cellular-level CARS images (upper panels) and the corresponding H&E staining results (lower panels) obtained from normal, adenocarcinoma, squamous cell carcinoma, and small-cell carcinoma human lung tissues. The normal lung mainly consists of well-organized fibrous elastin and collagen structures [shown as bright structures in Fig. 2(a)], and they work together to form a supporting network for the maintenance and integrity of lung tissues. Elastin constitutes up to 50% of the lung connective tissue mass and acts as the elastic protein allowing the lung tissue to resume its original shape after stretching. Collagen fibers are well-aligned proteins that provide support to maintain the tensile strength of lungs during the respiration process.<sup>57</sup> In contrast, cancerous lung tissues no longer preserve rich fibrous structures because cancer progression is often associated with the destruction and degradation of the original matrix network at the tumor invasion front.<sup>58,59</sup> Therefore, Figs. 2(b)–2(d) show much denser cellularity and significantly less fibrous structures compared with the normal samples. Because cell nuclei (yellow arrow) have less  $\text{CH}_2$  bonds compared to cell membrane and cytoplasm, they appear as dark spots in CARS images.

Commonly used pathological features can be identified in the three neoplastic lung types. Adenocarcinoma mostly contains

cancer cells that have nested large round shapes and vesicular nuclei, with inhomogeneous cytoplasm forming glandular structures.<sup>60</sup> Only a few broken elastin and collagen fibers are present in the tissue. Typical features in squamous cell carcinoma are pleomorphic malignant cells in sheets with abundant dense cytoplasm and formation of intracellular bridges.<sup>60</sup> Small-cell carcinoma is noted by round/oval cells with high nuclear–cytoplasmic ratio.<sup>61</sup> All CARS images illustrate good pathological correlation with H&E staining sections from the same tissue samples. Minor observed discrepancies between CARS and histology imaging and the inconsistent colors of H&E imaging were attributed to tissue fixation, processing, staining, and sectioning artifacts. The difficulty in locating the exact imaging spots due to the small FOV of CARS imaging and small working distance of the objective may also contribute to the mismatch between CARS and H&E imaging.

#### 3.2 Automatic Classification and Differential Diagnosis of Lung Tissues

We first validated the effectiveness of transfer learning on CARS images using a nine-fold cross-validation approach. The entire training and validation dataset was split into nine folds (folds are split into disjoint sets of patients). We held one fold at each time as the test set and trained the model on the remaining eight folds of the data, until each of the nine folds had served as the test set. The overall accuracy that the retrained model achieves is  $89.2\% \pm 2.1\%$  (mean  $\pm$  SD). The learning curves of training and validation for one cross-validation round displayed by TensorBoard are shown in Fig. 3. The stochastic gradient descent optimization algorithm was used to iteratively minimize the cost function. Sixty-four images were randomly picked in

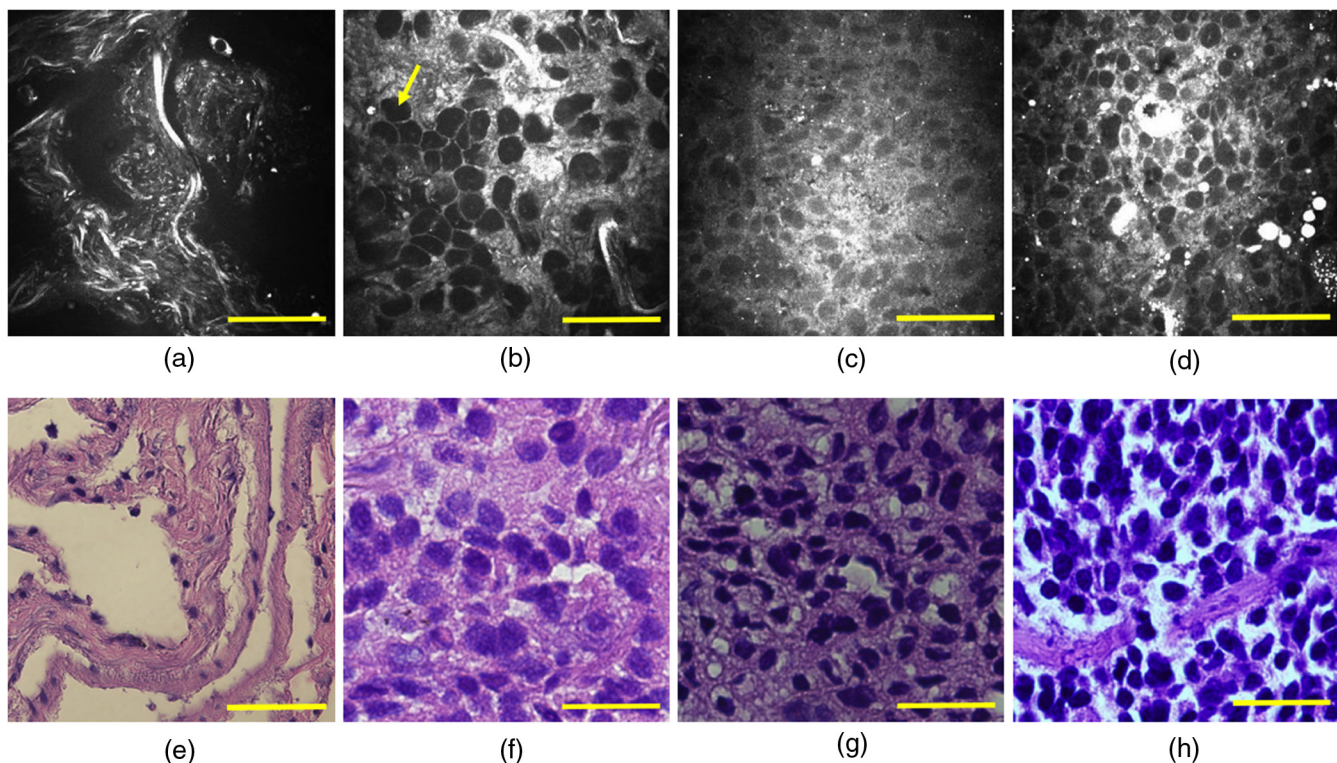


**Fig. 2** Representative CARS images (upper panels) and corresponding H&E-stained images (lower panels) of human lung tissues: (a) and (e) normal lung, (b) and (f) adenocarcinoma, (c) and (g) squamous cell carcinoma, and (d) and (h) small-cell carcinoma. Scale bars: 50  $\mu\text{m}$ .

each training step to estimate the gradient over all examples. The cost functions of training and validation in Fig. 3 both incline downward and converge to a low value after 40,000 steps.

We then tested the retrained model on the holdout test set that had never been seen by the model. The model also achieves 91.4% prediction accuracy, indicating its robustness to data. Figure 4(a) shows the normalized confusion matrix of our method on the holdout test set. Each row represents the instances in a ground-truth class and each column represents the instances predicted by the model. It can be noted that 100% of the actual normal cases are correctly classified as normal. 95% of the actual small-cell lung carcinoma cases are correctly labeled as small-cell lung carcinoma, only 4% of them are wrongly identified as nonsmall cell lung carcinoma. It is also worth mentioning that the two subtypes of NSCLC are sometimes misclassified as each other due to their morphological similarities, especially in poorly differentiated areas. This is in accordance with the challenges for pathologists in separating adenocarcinoma and squamous cell lung carcinoma.<sup>62</sup>

Given that the distribution of class labels in our dataset is not balanced, we plotted the receiver operating characteristic (ROC) curves [see Fig. 4(b)] for three conditions: (1) separating cancerous lung images from normal lung images; (2) separating small-cell carcinoma lung images from nonsmall cell carcinoma lung images; and (3) separating the subtypes of nonsmall cell carcinoma lung images, i.e., adenocarcinoma and squamous cell lung carcinoma. ROC curves feature false positive rate (1-specificity)

on the  $X$  axis and true positive rate (sensitivity) on the  $Y$  axis.<sup>63</sup> Specifically, “true positive” in each condition is: (1) the number of correctly predicted cancerous lung images; (2) the number of correctly predicted small-cell lung images; and (3) the number of correctly predicted adenocarcinoma lung images. When a test CARS image is fed through the model, the very last classification layer outputs a normalized probability distribution over four classes (normal, small-cell, adenocarcinoma, and squamous cell carcinoma). The ROC curve for each condition is created by plotting the true positive rate against the false positive rate at various discrimination thresholds. The area under the curve (AUC score) is also computed for each condition, whereas an AUC score close to 1 indicates an excellent diagnostic test. From a medical perspective, minimizing false negatives (known as type II error) is more important in cancer diagnosis because missing a cancerous case will lead to patients being untreated.

To better understand the internal features learned by the retrained model, we visualized the penultimate layer using t-distributed stochastic neighbor embedding (t-SNE) in Fig. 5.<sup>64,65</sup> Each point in Fig. 5 represents a CARS image from the holdout test set and the color represents its ground-truth label. The original 2048-dimensional output of the model’s last hidden layer is reduced and projected into a 2-D plane. t-SNE basically converts similarities between data points to joint probabilities and tries to minimize the Kullback–Leibler divergence between the joint probabilities of the low-dimensional embedding and the high-dimensional data.<sup>64</sup> The points that belong to the same class

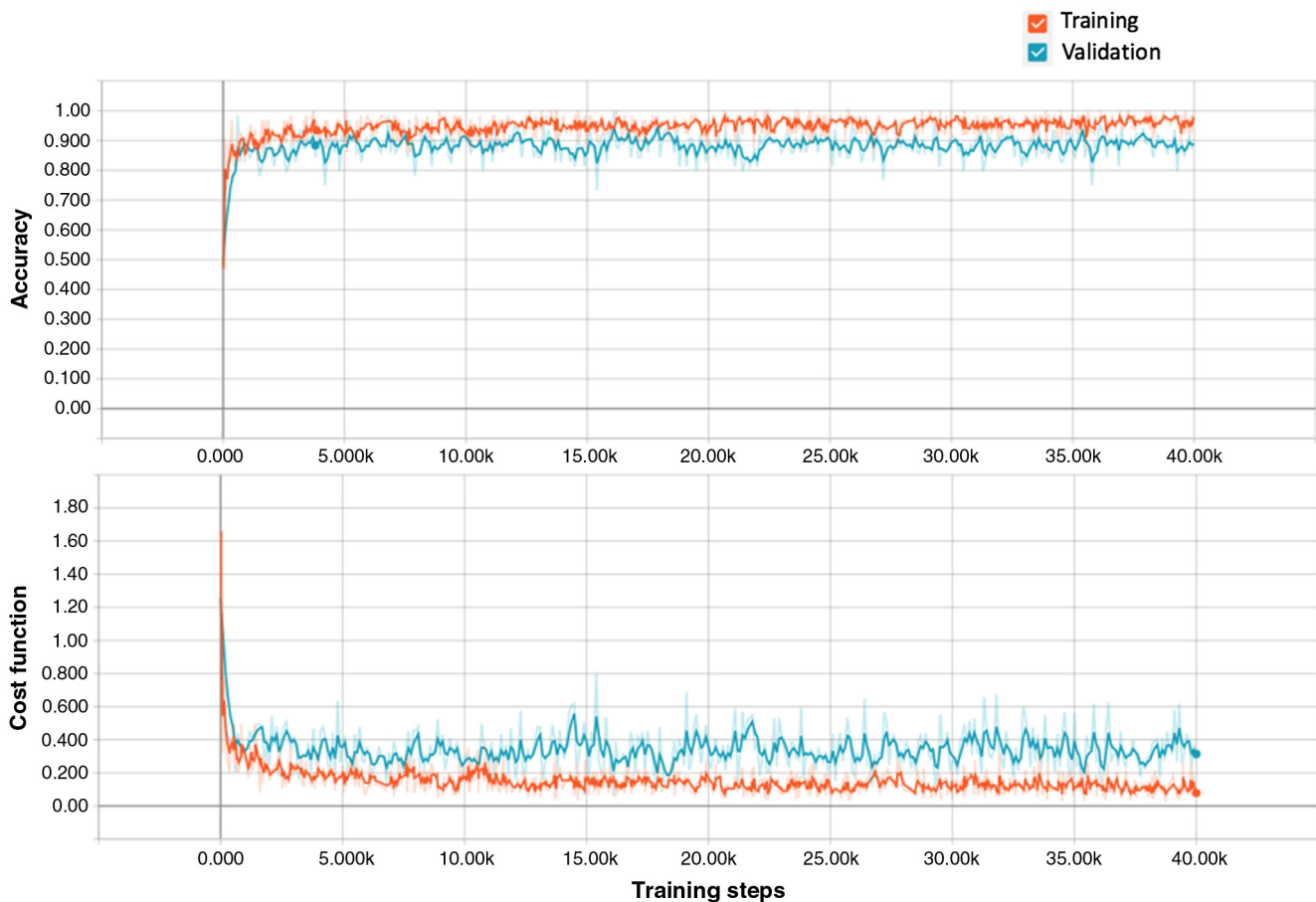


**Fig. 3** Learning curves of training and validation for one cross-validation round visualized by TensorBoard. The short-term noise is due to the stochastic gradient descent nature of the algorithm. The curves are smoothed for better visualization.

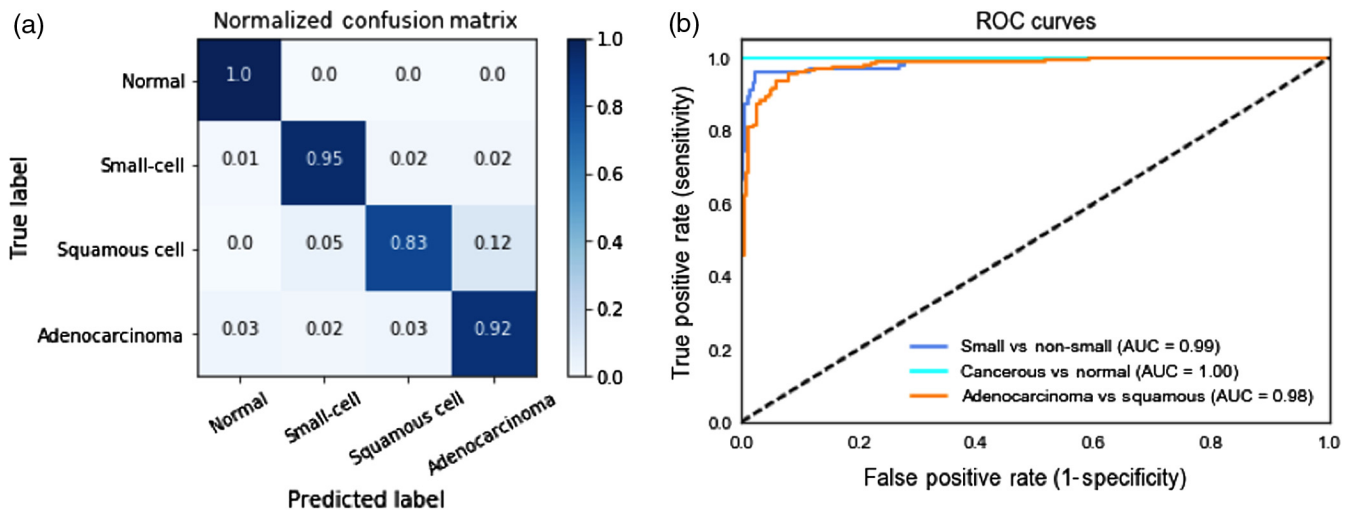


**Fig. 4** Deep CNN model performance on the holdout test set. (a) Normalized confusion matrix. Each row represents the instances in a ground-truth class and the value in each column represents what percentage of the images is predicted to a certain class. (b) ROC curves for three conditions: separating cancerous from normal lung images (light blue); separating small-cell carcinoma from nonsmall cell carcinoma lung images (dark blue); separating adenocarcinoma and squamous carcinoma lung images (orange). AUC scores are given in the legend.

should be clustered close together. As can be seen in Fig. 5, almost all the normal cases are grouped together clearly, which corresponds to the results in the confusion matrix. A few misclassified small-cell cases are located near the squamous cell carcinoma cases. Similarly, there exists some overlap between adenocarcinoma and squamous cell carcinoma as these two lung cancer subtypes have noticeable pathological similarities.

Neural networks have long been known as “black boxes” because it is difficult to understand exactly how any particular, trained neural network functions due to the large number of interacting, nonlinear parts.<sup>66</sup> In Fig. 6, we fed a normal and small-cell carcinoma CARS images into the model and visualized the first convolutional layer that consists of thirty-two kernels. Certain conventional image descriptors developed for object recognition can be observed in Fig. 6, such as detecting the edges of cell nuclei and detecting round lipid droplets. The

visualization of internal convolutional layers thus gives us better intuition on the convolutional operations inside the deep CNN model.

Finally, we proposed a majority voting strategy to further improve the performance of the model in predicting lung tissue classes. Since multiple CARS images at different imaging depths were acquired at each sampling point, we label the tissue type with the majority class to adjust the conflicting results among each z-stack. In the holdout test set, we correctly predict 8 out of 8 normal lung tissues, 4 out of 4 small-cell carcinoma lung tissues, 15 out of 16 adenocarcinoma lung tissues, and 9 out of 11 squamous cell carcinoma lung tissues. The overall prediction accuracy of this strategy is 92.3%, which is expected to be higher if we have more z-stacks for testing. This method gives more confidence in determining the tissue types without sacrificing too much time, as the acquisition of a z-stack normally takes less than a minute.

## 4 Discussion

Automating image analysis is essential to promoting the diagnostic value of nonlinear optical imaging techniques for clinical applications. Thus far, we have explored the potential of CARS imaging in differentiating lung cancer from nonneoplastic lung tissues and identifying different lung cancer types.<sup>16–18</sup> These strategies, however, are based on extraction and calibration of a series of disease-related morphology features. Therefore, they are not fully automatic because the quantitative measurement of the features requires the segmentation of cell nuclei, which involves a manual selection procedure and creates potential bias. In the superpixel-based 3-D image analysis platform, labeling the cell nuclei on all the images of one z-stack would take more than five minutes, which is very inefficient for analysis of a large amount of image data.

In this study, we exploited the recent advances in deep CNN and demonstrated how we can apply the model pretrained on the ImageNet data to a completely new domain such as CARS images and yet achieve reliable results. Our experimental results indicate that the proposed deep learning method has the

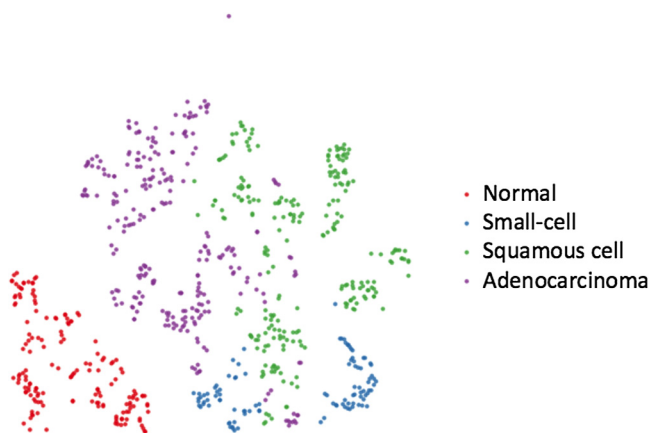


**Fig. 5** *t*-SNE visualization of the last hidden layer representations in the deep CNN of the holdout test set (758-CARS images). Colored point clouds represent four different human lung tissue classes clustered by the algorithm. Red points are normal lung images, blue points are small-cell carcinoma images, green points are squamous cell carcinoma images, and purple points are adenocarcinoma images.



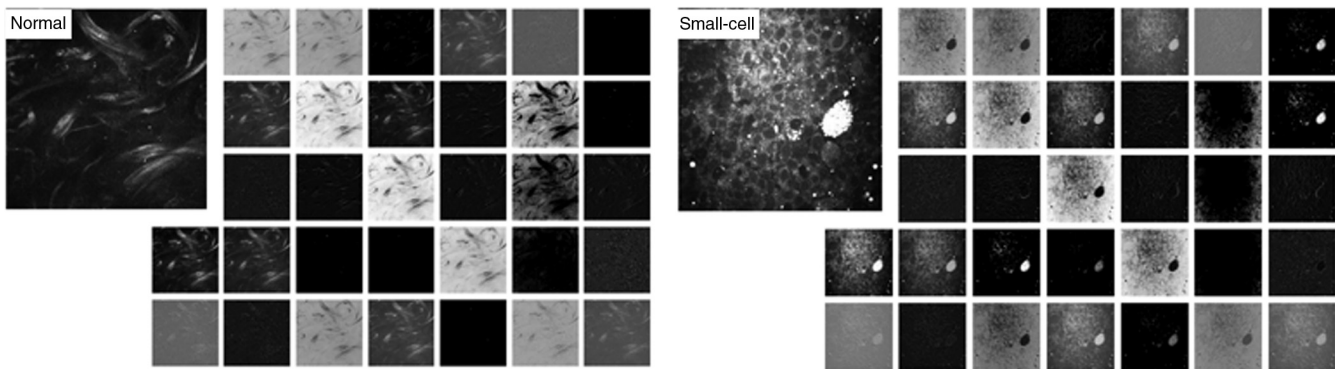


**Fig. 6** Visualization of the first convolutional layer in GoogleNet Inception v3 model for a normal and a small-cell lung carcinoma CARS images. The first convolutional layer contains 32 kernels with a size of  $149 \times 149$  pixels.

following advantages when coupled with label-free CARS images. First, deep CNN can extract useful features automatically,<sup>45</sup> thus we can use raw image pixel values directly as the input for the model. The algorithm described in this paper can label a batch of images quickly (0.48 s per image) without any preprocessing or human intervention. Second, we separated normal, small-cell carcinoma, adenocarcinoma, and squamous cell carcinoma lung CARS images using a single retrained model. In comparison, we previously built three different classifiers using three different feature sets in a hierarchical manner to separate normal from cancerous lung, small-cell carcinoma from non-small cell carcinoma, and adenocarcinoma from squamous cell carcinoma, respectively. Third, we used a larger dataset (7926 images as compared to previously  $\sim 1000$  images) and did not exclude the images that have blurry cell nuclei, as in a previous semiautomatic approach, resulting in a more robust model performance. Yet we still achieved comparable results to the previously reported results, i.e., 98.7% sensitivity and 100% specificity in separating cancerous from normal lung, 96.1% sensitivity and 96.2% specificity in separating small-cell carcinoma from non-small cell carcinoma, and 93.0% overall accuracy in separating adenocarcinoma from squamous cell carcinoma. Finally, in our previous works, we validated the performance of the classification algorithm using the leave-one-out method in which we repeatedly reserved one observation for prediction and trained the model on the rest of the dataset. However, this is a suboptimal validation method as compared

to the  $K$ -fold cross validation (in our method  $K = 9$ ), as it leads to higher variation in testing model effectiveness and it is computationally expensive when the size of the dataset is big.

We noticed that our CARS images have uneven background, most likely due to the chromatic aberrations. Interestingly, the traditional approach to remove background information of the microscopic images before feeding images into the deep CNN actually reduced the accuracy of prediction. This may be due to the fact that the background information contains subtle information about the foreground image features of interest, which normally are ignored by human inspectors. Meanwhile, it should be noted that most lung cancers are histologically heterogeneous among different patients, and the same cancer subtype may have different pathological characteristics at different stages, resulting much larger within-class appearance variations.<sup>60</sup> Figure 7 shows certain representative misclassified CARS images. Figure 7(a) is a false negative case where the model labels an adenocarcinoma image as normal, which may be caused by the fibrous structure (yellow arrow) that is rarely seen in cancerous tissues. This is called a type II error, which must be minimized in clinical practice. In Fig. 7(b), a squamous cell carcinoma is incorrectly classified as adenocarcinoma with a probability of 76%, indicating that the model is sometimes confused in differentiating adenoma and squamous cell carcinoma cases. In fact, separating NSCLC by visual inspection is also challenging for pathologists. In Fig. 7(c), a small-cell carcinoma is wrongly identified as squamous cell carcinoma. These mistakes might be induced by

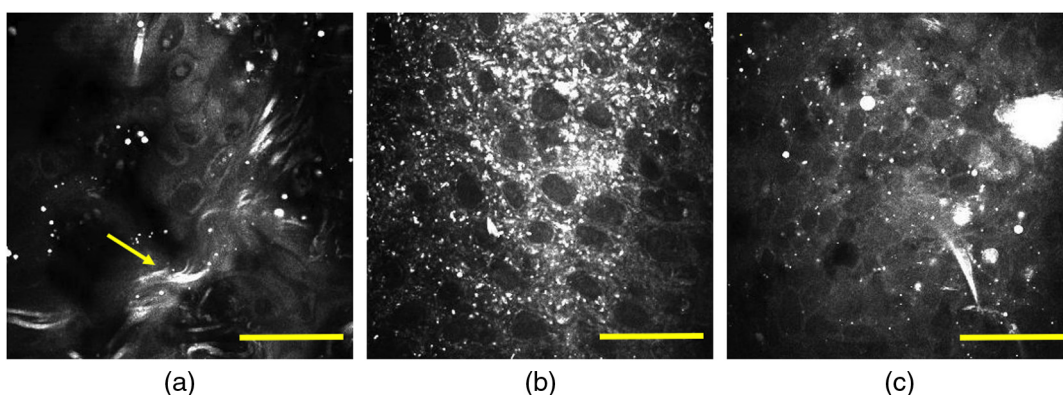


**Fig. 7** Representative CARS images of human lung tissues misclassified by the algorithm. (a) Adenocarcinoma is labeled as normal lung, (b) squamous cell carcinoma is labeled as adenocarcinoma, and (c) small-cell carcinoma is labeled as squamous cell carcinoma. Scale bars: 50  $\mu\text{m}$ .



the fact that these misleading images are minorities in the dataset, and consequently the model has not been well trained to label them correctly. Therefore, the best way to further improve the current performance is collecting more data that can cover a broader morphological spectrum of lung cancer tissues. Fine-tuning the hyperparameters across all the previous layers may also boost the model performance. However, the Inception v3 CNN contains about 5 millions tunable parameters and would thus require sufficiently large numbers of uniquely labeled images than our current method. Given the amount of data (before augmentation) and the computational resources available, we believe that leveraging the pretrained weights would be a more efficient solution than fine-tuning hyperparameters of the previous layers.

In the past decades, increasing attention has addressed developing minimized optical fiber-based CARS imaging probes for direct *in vivo* applications at clinical settings.<sup>67–70</sup> Our group has been studying the mechanisms of optical fiber delivered CARS,<sup>71–74</sup> and recently reported a fiber-based miniaturized endomicroscope probe design that incorporates a small lens part with microelectro-mechanical systems.<sup>75</sup> This device has opened up the possibility of applying CARS *in vivo* to provide reliable architectural and cellular information without the need for invasive and sometimes repetitive tissue removal. We expect that combining a miniaturized fiber optics probe and a deep learning-based automatic image classification algorithm will have the potential to detect and differentiate lung tissue on-the-spot during image-guided intervention of lung cancer patients and save precious time in sending tissue specimens for frozen sectioning diagnosis in a pathology laboratory. Furthermore, deep learning is agnostic to the type of images, thus it can be applied not only on CARS images, but also some other nonlinear optical imaging and microscopy imaging modalities, such as two-photon-excited autofluorescence (TPEAF) and second harmonic generation (SHG). We have proven that the morphological difference shown in TPEAF and SHG images can be used to differentiate normal and desmoplastic lung tissues.<sup>76</sup> A multimodal image classification algorithm can be developed in the future to incorporate with multimodal imaging techniques, such that more tissue structures can be detected and analyzed in real time.

In conclusion, we demonstrated the viability of analyzing CARS images of human lung tissues using a deep CNN that was pretrained on ImageNet data. We applied transfer learning to retrain the model and built a classifier that can differentiate normal and cancerous lung tissues as well as different lung cancer types. The average process time of predicting a single image is less than half a second. The reported computerized and label-free imaging strategy holds the potential for substantial clinical impact by offering efficient differential diagnosis of lung cancer, enabling medical practitioners to obtain essential information in real time and accelerate clinical decision-making. When coupled with a fiber-based imaging probe, this strategy would reduce the need for tissue biopsy while facilitating definitive treatment. This method is primarily constrained by data and can be further improved by having a bigger and more generalized dataset, to validate this technique across the full distribution and spectrum of lung lesions encountered in clinical practice.

## Disclosures

No conflicts of interest, competing or financial interests, or otherwise, are declared by the authors.

## Acknowledgments

We would like to thank Kelvin Wong, Miguel Valdivia Y Alvarado, Lei Huang, Zhong Xue, Zheng Yin, and Tiancheng He from the Department of Systems Medicine and Bioengineering, Houston Methodist Research Institute for helpful discussions. We would also like to thank Rebecca Danforth for proofreading this manuscript. The funding of this research was supported by NIH U01 188388, DOD W81XWH-14-1-0537, John S. Dunn Research Foundation, and Cancer Fighters of Houston Foundation.

## References

1. R. L. Siegel, K. D. Miller, and A. Jemal, "Cancer statistics, 2017," *CA. Cancer J. Clin.* **67**, 7–30 (2017).
2. D. R. Youlden, S. M. Cramb, and P. D. Baade, "The international epidemiology of lung cancer: geographical distribution and secular trends," *J. Thorac. Oncol.* **3**, 819–831 (2008).
3. A. McWilliams et al., "Innovative molecular and imaging approaches for the detection of lung cancer and its precursor lesions," *Oncogene* **21**, 6949–6959 (2002).
4. P. T. Cagle et al., "Revolution in lung cancer: new challenges for the surgical pathologist," *Arch. Pathol. Lab. Med.* **135**, 110–116 (2011).
5. C. I. Henschke et al., "Early lung cancer action project: overall design and findings from baseline screening," *Lancet* **354**, 99–105 (1999).
6. International Early Lung Cancer Action Program Investigators, "Survival of patients with stage I lung cancer detected on CT screening," *N. Engl. J. Med.* **2006**, 1763–1771 (2006).
7. M. Montaudon et al., "Factors influencing accuracy of CT-guided percutaneous biopsies of pulmonary lesions," *Eur. Radiol.* **14**, 1234–1240 (2004).
8. T. Gabrecht et al., "Optimized autofluorescence bronchoscopy using additional backscattered red light," *J. Biomed. Opt.* **12**, 064016 (2007).
9. B. Zaric et al., "Advanced bronchoscopic techniques in diagnosis and staging of lung cancer," *J. Thorac. Dis.* **5**, S359–S370 (2013).
10. A. Tremblay et al., "Low prevalence of high-grade lesions detected with autofluorescence bronchoscopy in the setting of lung cancer screening in the Pan-Canadian lung cancer screening study," *Chest J.* **150**, 1015–1022 (2016).
11. W. Denk, J. H. Strickler, and W. W. Webb, "Two-photon laser scanning fluorescence microscopy," *Science* **248**, 73–76 (1990).
12. G. Thomas et al., "Advances and challenges in label-free nonlinear optical imaging using two-photon excitation fluorescence and second harmonic generation for cancer research," *J. Photochem. Photobiol. B* **141**, 128–138 (2014).
13. D. Huang et al., "Optical coherence tomography," *Science* **254**, 1178–1181 (1991).
14. L. P. Hariri et al., "Diagnosing lung carcinomas with optical coherence tomography," *Ann. Am. Thorac. Soc.* **12**, 193–201 (2015).
15. H. Pahlevaninezhad et al., "Coregistered autofluorescence-optical coherence tomography imaging of human lung sections," *J. Biomed. Opt.* **19**, 036022 (2014).
16. L. Gao et al., "Differential diagnosis of lung carcinoma with coherent anti-Stokes Raman scattering imaging," *Arch. Pathol. Lab. Med.* **136**, 1502–1510 (2012).
17. L. Gao et al., "Differential diagnosis of lung carcinoma with three-dimensional quantitative molecular vibrational imaging," *J. Biomed. Opt.* **17**, 066017 (2012).
18. L. Gao et al., "On-the-spot lung cancer differential diagnosis by label-free, molecular vibrational imaging and knowledge-based classification," *J. Biomed. Opt.* **16**, 096004 (2011).
19. J.-X. Cheng and X. S. Xie, "Coherent anti-Stokes Raman scattering microscopy: instrumentation, theory, and applications," *J. Phys. Chem. B* **108**, 827–840 (2004).
20. C. L. Evans et al., "Chemical imaging of tissue *in vivo* with video-rate coherent anti-Stokes Raman scattering microscopy," *Proc. Natl. Acad. Sci. U. S. A.* **102**, 16807–16812 (2005).
21. J.-X. Cheng, A. Volkmer, and X. S. Xie, "Theoretical and experimental characterization of coherent anti-Stokes Raman scattering microscopy," *J. Opt. Soc. Am. B* **19**, 1363–1375 (2002).

22. R. Achanta et al., "SLIC superpixels," EPFL Technical Report, 149300, Switzerland (2010).
23. A. A. Hammoudi et al., "Automated nuclear segmentation of coherent anti-Stokes Raman scattering microscopy images by coupling super-pixel context information with artificial neural networks," in *Proc. of the Second Int. Conf. on Machine Learning in Medical Imaging*, pp. 317–325 (2011).
24. A. Lucchi et al., "Supervoxel-based segmentation of mitochondria in EM image stacks with learned shape features," *IEEE Trans. Med. Imaging* **31**, 474–486 (2012).
25. V. Kumar et al., "Robbins and Cotran pathologic basis of disease, professional edition e-book," Chapter 15 in *The Lung*, Elsevier Health Sciences (2014).
26. H. Abdi, "Partial least square regression (PLS regression)," *Encycl. Res. Methods Soc. Sci.* **6**, 792–795 (2003).
27. C. J. Burges, "A tutorial on support vector machines for pattern recognition," *Data Min. Knowl. Discovery* **2**, 121–167 (1998).
28. L. Gao et al., "Label-free high-resolution imaging of prostate glands and cavernous nerves using coherent anti-Stokes Raman scattering microscopy," *Biomed. Opt. Express* **2**, 915–926 (2011).
29. Y. LeCun, Y. Bengio, and G. Hinton, "Deep learning," *Nature* **521**, 436–444 (2015).
30. J. Schmidhuber, "Deep learning in neural networks: an overview," *Neural Networks* **61**, 85–117 (2015).
31. C. Szegedy et al., "Going deeper with convolutions," in *Proc. of the IEEE Conf. on Computer Vision and Pattern Recognition*, pp. 1–9 (2015).
32. M. Lin, Q. Chen, and S. Yan, "Network in network," ArXiv13124400 Cs (2013).
33. H. Wang and B. Raj, "On the origin of deep learning," ArXiv170207800 Cs Stat (2017).
34. M. A. Arbib, *The Handbook of Brain Theory and Neural Networks, Part 1: Background: The Elements of Brain Theory and Neural Networks*, MIT Press (2003).
35. J.-Z. Cheng et al., "Computer-aided diagnosis with deep learning architecture: applications to breast lesions in US images and pulmonary nodules in CT scans," *Sci. Rep.* **6**, 24454 (2016).
36. K. He et al., "Deep residual learning for image recognition," in *Proc. of the IEEE Conf. on Computer Vision and Pattern Recognition*, pp. 770–778 (2016).
37. A. Esteva et al., "Dermatologist-level classification of skin cancer with deep neural networks," *Nature* **542**, 115–118 (2017).
38. A. Krizhevsky, I. Sutskever, and G. E. Hinton, "ImageNet classification with deep convolutional neural networks," in *Advances in Neural Information Processing Systems* **25**, pp. 1097–1105 (2012).
39. D. Silver et al., "Mastering the game of Go with deep neural networks and tree search," *Nature* **529**, 484–489 (2016).
40. C. Szegedy et al., "Rethinking the inception architecture for computer vision," in *Proc. of the IEEE Conf. on Computer Vision and Pattern Recognition*, pp. 2818–2826 (2016).
41. S. Ioffe and C. Szegedy, "Batch normalization: accelerating deep network training by reducing internal covariate shift," in *Int. Conf. on Machine Learning*, pp. 448–456 (2015).
42. S. J. Pan and Q. Yang, "A survey on transfer learning," *IEEE Trans. Knowl. Data Eng.* **22**, 1345–1359 (2010).
43. J. Deng et al., "ImageNet: a large-scale hierarchical image database," in *IEEE Conf. on Computer Vision and Pattern Recognition*, pp. 248–255 (2009).
44. O. Russakovsky et al., "ImageNet large scale visual recognition challenge," ArXiv14090575 Cs (2014).
45. K. Simonyan and A. Zisserman, "Very deep convolutional networks for large-scale image recognition," ArXiv14091556 Cs (2014).
46. C. L. Evans and X. S. Xie, "Coherent anti-Stokes Raman scattering microscopy: chemical imaging for biology and medicine," *Annu. Rev. Anal. Chem.* **1**, 883–909 (2008).
47. Y. Yang et al., "Differential diagnosis of breast cancer using quantitative, label-free and molecular vibrational imaging," *Biomed. Opt. Express* **2**, 2160–2174 (2011).
48. T.-Y. Lin et al., "Microsoft coco: common objects in context," ArXiv Prepr. ArXiv14050312 (2014).
49. S. Xie et al., "Hyper-class augmented and regularized deep learning for fine-grained image classification," in *Proc. of the IEEE Conf. on Computer Vision and Pattern Recognition*, pp. 2645–2654 (2015).
50. R. Caruana, "Multitask learning," *Mach. Learn.* **28**, 41–75 (1997).
51. E. Ribeiro et al., "Transfer learning for colonic polyp classification using off-the-shelf CNN features," in *Int. Workshop on Computer-Assisted and Robotic Endoscopy*, pp. 1–13 (2016).
52. J. Chi et al., "Thyroid nodule classification in ultrasound images by fine-tuning deep convolutional neural network," *J. Digital Imaging* **30**, 477–486 (2017).
53. S. Hoo-Chang et al., "Deep convolutional neural networks for computer-aided detection: CNN architectures, dataset characteristics and transfer learning," *IEEE Trans. Med. Imaging* **35**, 1285–1298 (2016).
54. J. Shlens, "Train your own image classifier with Inception in TensorFlow," <https://research.googleblog.com/2016/03/train-your-own-image-classifier-with.html> (09 March 2016).
55. R. Hecht-Nielsen, "Theory of the backpropagation neural network," *Neural Networks* **1**, 445–448 (1988).
56. M. Abadi et al., "TensorFlow: large-scale machine learning on heterogeneous distributed systems," ArXiv160304467 Cs (2016).
57. M. Toshima, Y. Ohtani, and O. Ohtani, "Three-dimensional architecture of elastin and collagen fiber networks in the human and rat lung," *Arch. Histol. Cytol.* **67**, 31–40 (2004).
58. R. A. Cairns, R. Khokha, and R. P. Hill, "Molecular mechanisms of tumor invasion and metastasis: an integrated view," *Curr. Mol. Med.* **3**, 659–671 (2003).
59. T. Eto et al., "The changes of the stromal elastotic framework in the growth of peripheral lung adenocarcinomas," *Cancer* **77**, 646–656 (1996).
60. P. T. Cagle, R. Barrios, and T. C. Allen, "Color atlas and text of pulmonary pathology," Chapter 10 in *Carcinomas*, Lippincott Williams & Wilkins (2008).
61. R. Govindan et al., "Changing epidemiology of small-cell lung cancer in the United States over the last 30 years: analysis of the surveillance, epidemiologic, and end results database," *J. Clin. Oncol.* **24**, 4539–4544 (2006).
62. J. Terry et al., "Optimal immunohistochemical markers for distinguishing lung adenocarcinomas from squamous cell carcinomas in small tumor samples," *Am. J. Surg. Pathol.* **34**, 1805–1811 (2010).
63. T. Fawcett, "An introduction to ROC analysis," *Pattern Recognit. Lett.* **27**, 861–874 (2006).
64. L. van der Maaten and G. Hinton, "Visualizing data using t-SNE," *J. Mach. Learn. Res.* **9**, 2579–2605 (2008).
65. J. Donahue et al., "DeCAF: a deep convolutional activation feature for generic visual recognition," in *Int. Conf. on Machine Learning*, pp. 647–655 (2014).
66. J. Yosinski et al., "Understanding neural networks through deep visualization," ArXiv Prepr. ArXiv150606579 (2015).
67. B. G. Saar et al., "Coherent Raman scanning fiber endoscopy," *Opt. Lett.* **36**, 2396–2398 (2011).
68. M. Balu et al., "Fiber delivered probe for efficient CARS imaging of tissues," *Opt. Express* **18**, 2380–2388 (2010).
69. S. Murugkar et al., "Miniaturized multimodal CARS microscope based on MEMS scanning and a single laser source," *Opt. Express* **18**, 23796–23804 (2010).
70. F. Légaré et al., "Towards CARS endoscopy," *Opt. Express* **14**, 4427–4432 (2006).
71. Z. Wang et al., "Coherent anti-Stokes Raman scattering microscopy imaging with suppression of four-wave mixing in optical fibers," *Opt. Express* **19**, 7960–7970 (2011).
72. Z. Wang et al., "Delivery of picosecond lasers in multimode fibers for coherent anti-Stokes Raman scattering imaging," *Opt. Express* **18**, 13017–13028 (2010).
73. S. Weng et al., "Dual CARS and SHG image acquisition scheme that combines single central fiber and multimode fiber bundle to collect and differentiate backward and forward generated photons," *Biomed. Opt. Express* **7**, 2202–2218 (2016).
74. Z. Wang et al., "Use of multimode optical fibers for fiber-based coherent anti-Stokes Raman scattering microendoscopy imaging," *Opt. Lett.* **36**, 2967–2969 (2011).
75. X. Chen et al., "Multimodal nonlinear endo-microscopy probe design for high resolution, label-free intraoperative imaging," *Biomed. Opt. Express* **6**, 2283–2293 (2015).
76. X. Xu et al., "Multimodal non-linear optical imaging for label-free differentiation of lung cancerous lesions from normal and desmoplastic tissues," *Biomed. Opt. Express* **4**, 2855–2868 (2013).

**Sheng Weng** received his PhD in applied physics from Rice University and his BSc degree in physics from Zhejiang University. He is a data scientist at Amazon. His research interests include translational biophotonics imaging, image processing and recognition, and machine learning.

**Xiaoyun Xu** is a research associate at Houston Methodist Research Institute. She received her PhD in chemistry from the University of Utah. Her research interests include label-free optical imaging for early detection and accurate diagnosis of cancer.

**Jiasong Li** is a postdoctoral fellow at the Houston Methodist Research Institute. He has published more than 30 peer-reviewed

journal articles since his PhD study. His research is focused on the developments and applications of optical imaging systems, data analysis, and signal processing.

**Stephen T. C. Wong** is a John S. Dunn presidential distinguished chair of Houston Methodist Research Institute, a chair of the Department of Systems Medicine and Bioengineering at Houston Methodist Research Institute, and a professor at Weill Cornell Medicine. His research applies systems biology, AI, and imaging to solve complex disease problems.